Acoustic study of $YBa_2Cu_3O_x$ thin films

Soon-Gul Lee, Cheng-Chung Chi, Gad Koren, and Arunava Gupta

IBM Research Division, Thomas J. Watson Research Center, P. O. Box 218, Yorktown Heights, New York 10598

The attenuation of surface acoustic waves by epitaxial $YBa_2Cu_3O_x$ films has been studied for $x \simeq 6$ to 7. For fully oxygenated samples, the acoustic attenuation as a function of temperature shows two broad peaks at about 135 and 240 K, and decreases monotonically below the lower peak temperature. The cause of attenuation peaks is attributed to scattering by optical phonons. Our data do not show any gap structure at T_c due to relatively weak electron-phonon interactions at the acoustic frequencies. As the oxygen deficiency increases, the temperature dependence of the dc resistance changes from metallic to semiconducting and finally to insulating behavior. Acoustic attenuation data correspondingly show a drastic change due to different attenuation mechanisms: from the phonon scattering loss in the metallic regime to the electric-field coupling loss in the semiconducting and insulating regimes. In the latter regimes, the temperature dependence of low-frequency resistance calculated from the attenuation data can be fitted to a three-dimensional Mott variable-range-hopping model.

I. INTRODUCTION

Since the discovery of high-temperature superconductors, a great deal of effort has been made toward both applications and fundamental understandings of numerous unusual behaviors. Although some progress has been seen in both areas, a consensus picture of the mechanism is still to be established. Most of the experimental difficulties originate from the extremely short coherence length which is of the order of the unit cell. Defects of microscopic scale can cause large variations in experimental results from sample to sample. Thus, it is difficult to interpret such experimental results.

Ultrasonic attenuation has been one of the classic measurements to determine the energy gap in low-temperature superconductors.[1,2] Usually, tunnel-junction measurement provides the most accurate determination of the energy gap. But, due to the extremely short coherence length of high-T_c superconductor oxides, reproducible high-quality junctions have yet to be realized for a reliable energy-gap measurement. Naturally the acoustic technique, which is essentially a bulk probe, has been explored to study the oxide superconductors. Unfortunately, the acoustic technique encounters a different difficulty. The usual pulse-echo technique requires a large homogeneous sample of the order of centimeters in size. Good high-T_c single crystals are usually much smaller than that. Thus, most of the acoustic measurements have been done with sintered ceramic samples. Reported data on ceramic samples show a large variation from sample to sample.[3-5] This is not surprising because porosity and process-dependent intergrain material can cause a large phonon scattering background and thus cause sample-to-sample variations. Nontheless, several broad peaks in the acoustic attenuation versus temperature curve have been repeatedly observed. To get around the difficulty of dealing with small samples, there have

been a couple of reports on acoustic measurements of single crystals using different techniques. Saint-Paul et al.[6] used a conventional echo technique with a quartz buffer rod. They reported a gradual reduction of acoustic attenuation with decreasing temperature without any peak. On the other hand, using a vibrating-reed technique, Shi et al.[7] reported such peaks in a single crystal as often observed in bulk ceramic samples. Very recently, Kim et al.[8] have reported measurements on relatively large single crystals using a conventional echo technique. They have observed similar peaks for transverse C_{44} modes. None of the experiments on either ceramic samples or single crystals have clearly indicated a superconducting gap below the superconducting transition temperature.

In this paper we report results of an experimental acoustic attenuation study of $YBa_2Cu_3O_7$ thin films epitaxially grown on $LiNbO_3$ substrates using a surface-acoustic-wave (SAW) technique. We note that a similar technique has been previously used to study superconducting Pb and Sn films.[9] We have also studied systematically the effects of oxygen deficiency on the acoustic attenuation. All previous measurements are limited to fully oxygenated samples.

II. EXPERIMENT

Depositing high quality films on SAW substrates is very important to get meaningful results from SAW attenuation experiments. Otherwise interfacial coupling and intergranular material will severely affect the experimental results. Our ability to fabricate high quality epitaxial $YBa_2Cu_3O_7$ films on Y-cut $LiNbO_3$ substrates, which are widely used for SAW devices, has been demonstrated.[10] There are certain advantages of the SAW attenuation technique over others. First of all, large homogeneous samples are available. Also, the whole spectrum of effects of oxygen deficiency can be studied systemati-

cally for a given sample without degrading the sample quality.

Fully oxygenated films are deposited *in situ* on Y-cut LiNbO$_3$ substrates by a standard laser ablation technique.[10] Typical film thickness is on the order of 1 μm and the films are visually smooth. Under an optical microscope, typically submicronsized particulates are found. A scanning-electron-microscope (SEM) study conducted for one of the samples indicates a partial columnar growth of the film. Film epitaxy and orientation are determined by x-ray diffraction study. The relative orientation of the film to the substrate is illustrated in Fig. 1. The c axis of the film is perpendicular to the substrate plane and the [110] direction of the film is parallel to the [11$\bar{2}$0] orientation or z axis of the LiNbO$_3$ substrate, which has a trigonal symmetry. The films have two domains, with the (110) plane acting as a mirror plane. Details of the x-ray diffraction study have been described in Ref. 10. As indicated by the SEM study, the films are not single crystalline but consist of small crystalline plaquettes which are typically of micron size with all three crystal axes oriented as described above.

Figure 2 shows results of resistivity and critical current density measurements of a 0.2-μm thick film. In Fig. 2, as temperature decreases, normal-state resistivity decreases with a slight curvature and drops to zero at 92 K. The room-temperature resistivity of this film is 750 $\mu\Omega$ cm, which is rather high for an epitaxial film. The critical current densities are 2×10^5 A/cm^2 at 77 K and 8×10^5 A/cm^2 at 4.2 K, in accordance with the epitaxial nature of the film. Several thicker films, typically 1 μm thick, have also been measured and showed much lower room-temperature resistivity (about 250 $\mu\Omega$ cm), as well as a much stronger and more linear temperature dependence in the resistivity.

A schematic diagram of the experimental set-up for the SAW attenuation measurement is shown in Fig. 3. Before the deposition of the YBa$_2$Cu$_3$O$_7$ film, three identical interdigital transducers made of Au or Pt are patterned

FIG. 2. Resistivity and critical current density of a 0.2-μm thick, 50×200-μm^2 laser patterned line of the film.

FIG. 3. Schematic diagram of experimental set-up for the acoustic measurement. x, y and z coordinates indicate the crystallographic axes of the LiNbO$_3$ substrate. $A-D$ represent analog-to-digital converter.
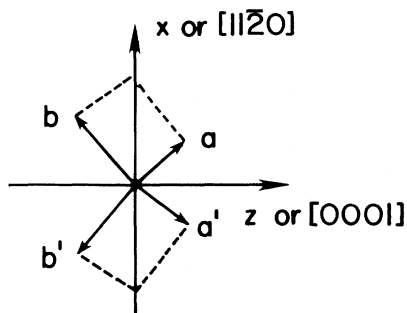

FIG. 1. Orientation of the film with respect to the substrate. a and b, a' and b' are axes of the film in the basal plane in two different domains. x and z are axes of the substrate. The c axis of the film and y axis of the substrate are perpendicular to the plane.
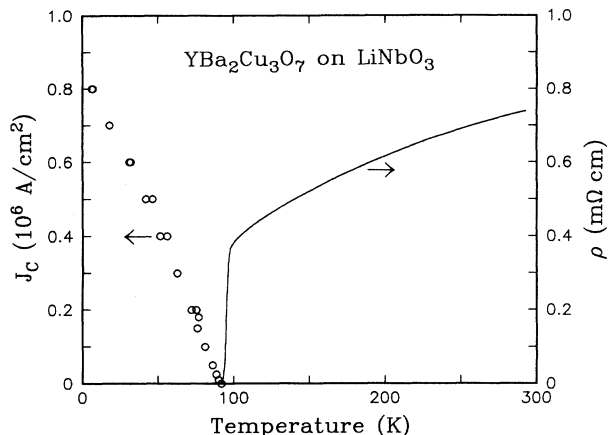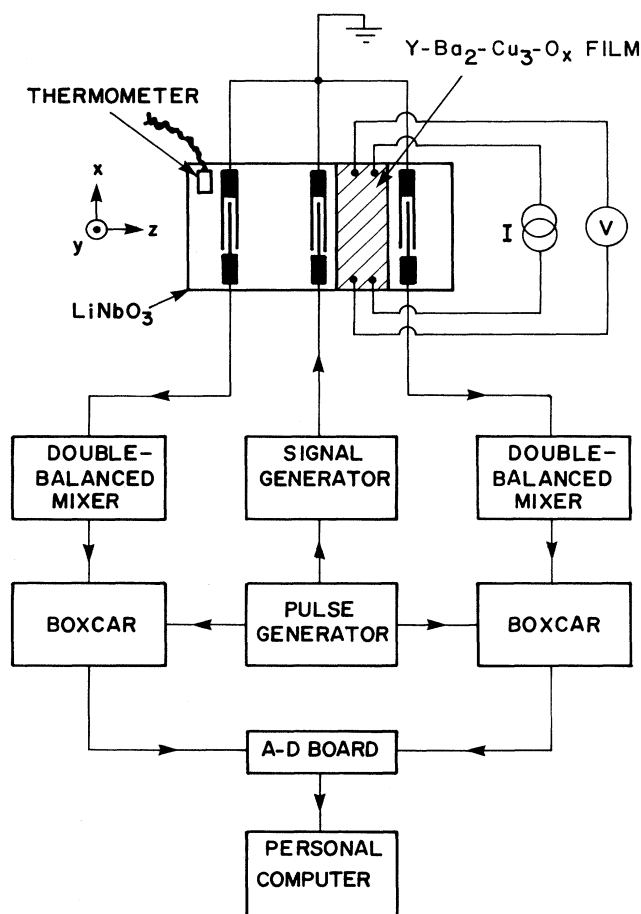
on the Y-cut LiNbO$_3$ substrates with equal spacings of 6 mm. The transducers are designed for 29-MHz SAW's. The width of the electrode is 10 μm and the gap between nearest electrodes is 50 μm. Each transducer has 10 pairs of electrodes. The center transducer serves as a SAW generator and the end sets as receivers. A YBa$_2$Cu$_3$O$_7$ film of $\sim$1-μm thickness and 3–4-mm width is deposited between the generator and one of the receivers. Thus, one receiver detects the signal through both the film and substrate, and the other one detects the signal through the bare substrate. The latter is used as a reference to normalize out any substrate effect. A cold finger cryostat is used to control the sample temperature in a vacuum environment. The cryostat is equipped with three thin gold-braided coaxial cables for rf signals and several pairs of twisted wires for dc resistance measurement and thermometry.

SAW's are generated by applying 29-MHz sinusoidal waves gated by a pulse generator to the center transducer. The gate pulse has typically a 0.5–1-μs width and a 100-μs period. Pulse trains of SAW's produced by the generator propagate in both directions and are detected by the two receivers. The signal detected by each group of fingers is self-mixed, amplified, and integrated by a box car, and finally digitized and recorded by a personal computer. The SAW attenuation of the film is obtained by dividing the signal traveling through the sample arm by that of the reference arm. The result is then substracted from unity. Signals can be complicated by reflections from the edges of the substrate. We have avoided this problem by making both end surfaces rough and by lengthening the pulse period. The sample temperature is monitored by a Si diode thermometer mounted on the substrate. Both SAW signals and the dc resistance of the film are measured simultaneously as the substrate temperature is slowly ramped up or down between room temperature and 4.2 K.

We have studied eight samples. Among those, we present two representative samples labeled $S1$ and $S2$. Those two samples are among the best in terms of normal-state resistivity and T_c. They have been studied most comprehensively. The results for samples $S1$ and $S2$ are shown in Figs. 4 and 5. Both samples have resistivities of about 250 $\mu\Omega$ cm at room temperature with steep slopes, indicative of high quality. Even though the character of their resistive transition is similar, the SAW attenuation data differ. While sample $S1$ has two broad peaks at about 135 and 240 K, sample $S2$ has a monotonic decrease with decreasing temperature. About half of the samples studied showed the same behavior as $S1$ (with some variation in the peak height), while the other half were similar to $S2$. The latter have larger attenuation than the former, as shown in Figs. 4 and 5. In the latter group, the peaks observed in the former are overshadowed by a large monotonic background. In some sense, our results are a miniature scope of what has been published in literature for bulk ceramics and single crystals. There does not seem to be any strong correlation between SAW attenuation and dc resistivity or T_c. It is likely that different intergranular interactions or microscopic crystalline defects can cause different high-
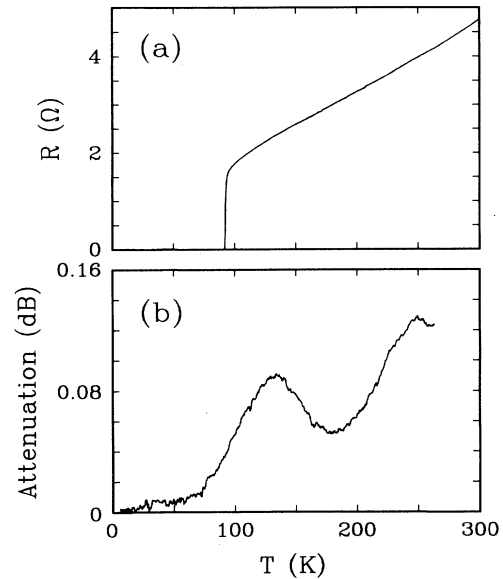

FIG. 4. Results for sample $S1$ in the fully oxygenated state. (a) Resistance vs temperature. (b) Acoustic attenuation vs temperature.

frequency responses and thus different SAW attenuation background without affecting the dc resistance or T_c.

One of the advantages of using thin films is that annealing times are much shorter than that for single crystals. Typically, annealing takes only a few hours for thin
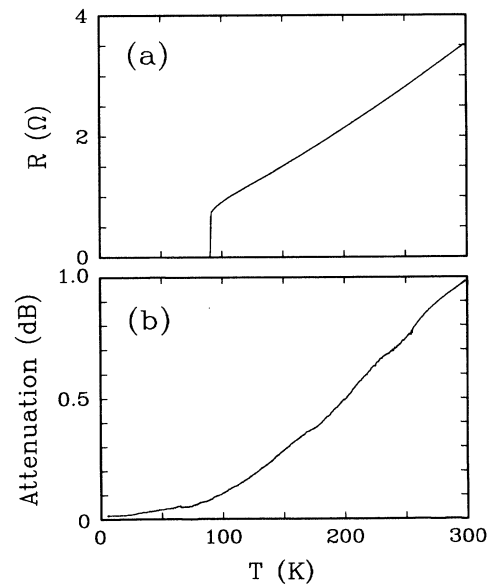

FIG. 5. Results for sample $S2$ in the fully oxygenated state. (a) Resistance vs temperature. (b) Acoustic attenuation vs temperature.

films rather than a few weeks for single crystals. We have studied the effects due to the oxygen deficiency of the same sample by annealing out oxygen gradually and repeating measurements after each annealing. The annealing is done in a quartz tube furnace at 500 °C. One end of the tube is pumped by an oil-free turbomolecular pump with a small amount of oxygen gas introduced from the other end. The oxygen concentration of the films is controlled by adjusting the oxygen flow rate. During annealing, the film resistance is indirectly monitored by measuring the resistance of a separate $YBa_2Cu_3O_x$ film placed near the sample. The sample is annealed until the resistance of the monitor film reaches a steady-state value. We have found that as more oxygen is depleted, the required annealing time becomes longer. It is on the order of 30 min in the metallic regime and several hours near the insulating regime.

For bulk ceramic samples, the thermogravimetric method is commonly used to determine oxygen content. For films on substrates, the weight loss due to oxygen depletion is far too small to be measured, and thus the c-axis lattice constant determined from the x-ray diffraction pattern has been used to indirectly infer the oxygen content. The c-axis lattice constant of our films were measured after each annealing step. Oxygen concentration of the film for each step is inferred from the relationship between oxygen content and the c-axis lattice parameter for powdered ceramic samples.[11,12] The measured c-axis constant and estimated oxygen content for sample $S2$ are shown in Table I. Notice that the c-axis for the fully oxygenated film is 11.71 Å, which is substantially larger than 11.68 Å for powdered samples. This indicates that the film is strained due to the severe lattice mismatch. As shown in Table I, with decreasing oxygen concentration, the room-temperature resistance increases monotonically. Cava et al.[11] have measured room-temperature resistivity versus oxygen concentration for powdered ceramic samples. Their data have a local minimum for the 60-K phase. But the resistivity minimum does not appear in our film sample. The oxygen extraction process is reversible. The oxygen in the

sample can be completely replenished by annealing at 500 °C at atmospheric pressure in pure oxygen. Both the resistance and SAW attenuation data of the reoxygenated film are nearly identical to those of the virgin sample. Also, x-ray studies after several annealing steps have not shown any sign of the development of secondary phases.

Measured dc resistance versus temperature curves for the nine different oxygen concentrations in Table I are plotted in Fig. 6. As oxygen content decreases, T_c decreases and in F no transition is observed. Temperature dependence of the normal-state resistance shows metallic behavior for A to E, semiconducting behavior for F to H, and finally insulating behavior for I, for which no dc resistance measurement is available due to high contact resistance. In semiconducting states F and G, the resistance curve cannot be fitted to a simple exponential function characteristic to typical semiconductors. Curve G is somewhat unusual. The resistance decreases below 40 K and eventually flattens at low temperatures. Orr et al.[13] have measured temperature-dependent resistances of nearly percolating ultrathin Sn films. Their data show

TABLE I. Sample parameters for different oxygen concentrations of sample $S2$.

	$R_{300K}(\Omega)$	$c(\text{Å})^a$	x^b
A	4.8	11.71	6.83
B	8.7	11.72	6.78
C	16	11.74	6.60
D	25	11.76	6.47
E	82	11.81	6.14
F	800	11.80	6.22^c
G	1.7×10^3	11.85	5.90
H	1.8×10^5	11.82	6.17^c
I	$> 10^7$	11.87	5.76

[a]Error bar is ± 0.01 Å.
[b]Estimated by using the results of powdered sample (Refs. 11 and 12).
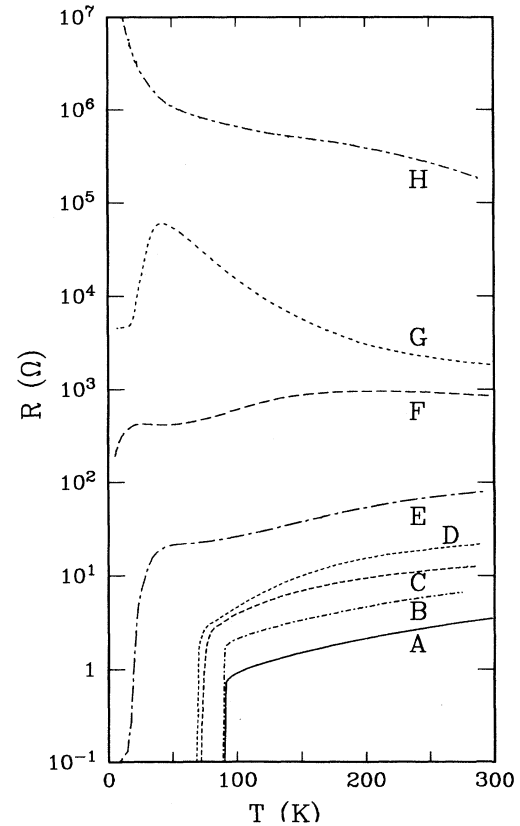[c]Measured after several months from the rest.

FIG. 6. Resistance vs temperature for different oxygen concentrations of sample $S2$. Indices A to I indicate oxygen concentrations from the fully oxygenated state to a nearly insulating state, as shown in Table I. Notice that resistance scale is logarithmic.

similar behavior at low temperatures. There have been several reports on the ordering of oxygen vacancy in YBa$_2$Cu$_3$O$_x$ systems.[14,15] even an ideal sample which is annealed homogeneously might have an intrinsically inhomogeneous oxygen distribution because of the vacancy ordering. Thus, we speculate that the resistance drop in G is due to percolation between superconducting grains.

SAW attenuation data for different oxygen contents are shown in Fig. 7. Data can be divided into two groups. For the first group, A to E, the acoustic attenuation is relatively small and has a monotonic temperature dependence. For the other group, F to I, the attenuation is much larger and has a broad peak, which shifts toward higher temperature as the sample becomes more insulating. B, C, and D, which lie in between A and E are omitted from Fig. 7 for clarity. The attenuation mechanisms of these two groups will be discussed in the next section.

III. MECHANISMS OF SAW ATTENUATION

There are intrinsic differences between the SAW technique and bulk acoustic wave techniques. Unlike bulk waves used in the echo technique, SAW's inherently have

both longitudinal and transverse components coupled together.[16] In our case, SAW's propagate along the z axis of the substrate, which is roughly parallel to the diagonal direction of the ab plane of the high T$_c$ films. Consequently our observed SAW attenuation is an average over all three axes, similar to the case of bulk acoustic attenuation in randomly oriented ceramics, but without the complications of voids and intergranular materials. Another important difference is that a relatively large electric field accompanies SAW's due to the piezoelectric effect of the substrate. The loss due to the electric field coupling can be an important SAW attenuation mechanism for highly resistive thin films.

The electric field coupling effect can be interpreted by a transmission-line model, as shown in Fig. 8. Compression and rarefraction of the substrate generate electric fields. The electric field is described in terms of an electric potential V which oscillates in time and space with a frequency ω. For a perfectly conducting film ($R = 0$), the electrical charge induced in the film oscillates in phase with the field and does not dissipate the SAW's. The extra capacitance due to the film causes a reduction in the SAW velocity. For a resistive film ($R \neq 0$), the oscillation of the induced charge has an out-of-phase component, which causes SAW attenuation by producing Joule heating in the film. This electric field effect is well understood. For films with thickness $d \ll v_s / \omega$, the attenuation α can be expressed as[16,17]

$$\alpha \lambda = \pi K^2 \frac{v_s \epsilon_s R_\square}{1 + (v_s \epsilon_s R_\square)^2} , \tag{1}$$

where λ is the SAW wavelength, K^2 is the piezoelectric coefficient of the substrate, v_s is the SAW velocity, ϵ_s is the dielectric constant of the substrate, and $R_\square$ is resistance per square of the film. For Y-cut LiNbO$_3$ substrates, $v_s = 3500$ m/sec, $\epsilon_s = 4.6$ pF/cm, and $K^2 = 0.046$ (Ref. 16). In Fig. 9, the SAW attenuation due to electric field coupling calculated using Eq. (1) is plotted as a function of the resistance per square of the film for our sample with a width of 30λ. As shown in the figure the SAW attenuation reaches a maximum of 19 dB at $R_\square = 1 / v_s \epsilon_s = 620$ kΩ. The field-coupling effect becomes
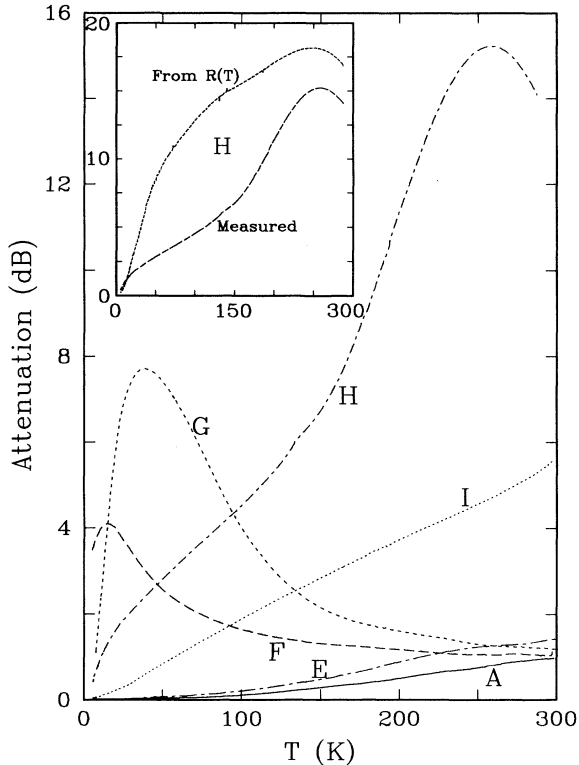

FIG. 7. Temperature-dependent acoustic attenuation curves for different oxygen concentrations of sample S2. Indices are the same as in Fig. 6 and Table I. In the inset, the calculated SAW attenuation curve for the state H [using Eq. (1) with the measured $R_\square(T)$] is plotted together with the measured one.
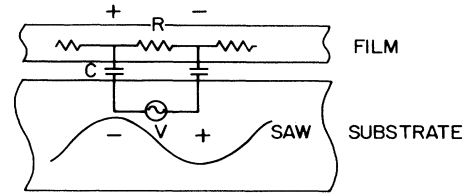

FIG. 8. Transmission-line model of SAW attenuation due to electric field coupling loss. In the figure, there is a gap between the film and the substrate for clarity. Capacitance C is determined by the dielectric constant of the substrate ϵ_s. The induced charge density in the film has out-of-phase component with respect to the SAW's because of RC coupling.

less important toward both metallic and insulating regimes, where SAW attenuation is proportional to $R_\square$ and $1/R_\square$, respectively.

In the metallic state, electron-phonon scattering is an important acoustic loss mechanism. In the conventional metal superconductors, it dominates acoustic attenuation at low temperatures and provides valuable information concerning the superconducting gap via the temperature dependence of the acoustic attenuation below T_c.[18] The magnitude of the acoustic attenuation due to electron-phonon scattering is[19]

$$\alpha\lambda \approx 4\pi^2 \frac{nmv_F}{\mu v_s} \frac{l}{\lambda} . \tag{2}$$

Here, m is the effective electronic mass, n is the electron density, and μ is the mass density of the lattice. v_F and v_s are Fermi velocity and sound velocity, respectively, and l is the electron mean free path. Note that the acoustic attenuation due to electron-phonon coupling is proportional to $1/R_\square$, in contrast to a proportionality to $R_\square$ for the electric field coupling loss. In case of thin films, the SAW attenuation is reduced from the above value by d/λ because only a portion d/λ of the SAW's is affected by the films. For typical high-temperature superconducting thin films in the fully oxygenated state, the SAW attenuation due to the electron-phonon interaction (estimated using the literature parameters[20]) is roughly 10^{-6} dB, about 2

orders of magnitude smaller than the field coupling loss. The electron-phonon interaction is overwhelmed by the electric field coupling. But, even the field coupling loss is 3–4 orders of magnitude smaller than the data, which are typically 0.1–1 dB in the fully oxygenated state (Figs. 4 and 5). Moreover, Eq. (1) indicates that the field coupling loss vanishes below T_c, while data show substantial attenuation. Thus, the SAW attenuation mechanism in the fully oxygenated state cannot be either the electron-phonon interaction or the electric field coupling loss.

In Figs. 6 and 7 the SAW attenuation is seen to increase with increasing film resistance, reaching a maximum in H, and then decreasing again with further increase of the film resistance in I, in a qualitative agreement with Eq. (1). Using the maximum of the curve H in Fig. 7, we can quantitatively compare acoustic data with the model. The attenuation curve calculated from dc resistance data H in Fig. 6 using Eq. (1) is plotted along with measured attenuation curve H in the inset of Fig. 7. In the calculation, $v_s \epsilon_s$ is used as a fitting parameter and the result is $(270 \text{ k}\Omega)^{-1}$. This is not unreasonable because near the interface between film and substrate, the dielectric properties might be modified. Notice that the calculated curve agrees reasonably well with the measured curve both in magnitude and temperature dependence. For the less oxygen deficient states F and G, the measured values of attenuation (Fig. 7) are much larger than the ones estimated using $\alpha w(R_\square)$ (Fig. 9) and resistance data (Fig. 6). The discrepancies may be explained as follows. While the dc resistance is determined by connectivity of conducting paths, the acoustic attenuation probes the average bulk properties. Thus, we can conclude that the states F and G might have an inhomogeneous oxygen distribution .

One of the important questions about the acoustic attenuation measurements is whether the electron-phonon interaction or the superconducting gap can be obtained. Up to the present, none of the reports on acoustic attenuation of oxide superconductors have demonstrated any gap structure. Our results are consistent with the other studies. An estimation using Eq. (2) indicates that the electron-phonon effect is several orders of magnitude smaller than what is actually observed in our samples. Moreover, as indicated by Eq. (2), acoustic attenuation by the electron-phonon interaction is proportional to conductivity, which is opposite to our observation (Figs. 4 and 5) that both resistance and acoustic attenuation decrease with decreasing temperature. This suggests that the acoustic attenuation in high-temperature superconductors is dominated by mechanisms other than the electron-phonon interactions.

IV. DISCUSSION AND CONCLUSION

Several explanations have been suggested for the two broad peaks observed at about 135 and 240 K in Fig. 4 (Refs. 3, 5, 7, and 8). Since the energy of the acoustic phonons used in our experiment is very low (equivalent to a thermal energy of 10 mK), they cannot induce any excitation. They are either scattered or absorbed by existing excitations. We believe that the two broad peaks result
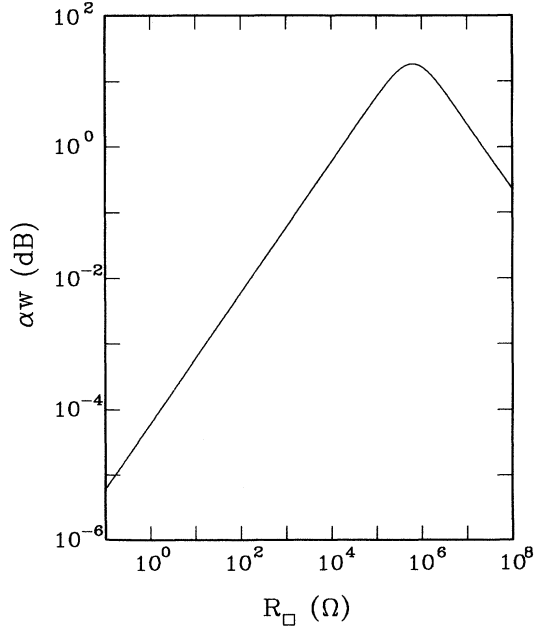

FIG. 9. SAW attenuation for our sample geometry as a function of resistance per square of the film. w is the length of the film through which SAW's propagate.

from scattering by phonon modes. Several optical pho-
non modes have been observed from infrared measure-
ments in the tetragonal phase of YBa$_2$Cu$_3$O$_x$ near 110
cm^{-1} and near 160 cm^{-1} (Ref. 21), which correspond to
about 160 and 230 K, respectively. In the orthorhombic
phase, lower frequency modes are not observed in the IR
measurement due to the screening by free charge car-
riers.[22] Acoustic waves penetrate much deeper into the
sample and thus can interact with those modes in the ful-
ly oxygenated samples. The normal modes correspond-
ing to these peaks have not been clearly identified. It is
believed that the heavy Ba atoms are involved.[21] Scatter-
ing of acoustic waves by optical phonons is possible only
if both thermally excited phonons and anharmonicity ex-
ist in those modes. The scattering rate increases with in-
creasing anharmonicity. If the anharmonicity is indepen-
dent of temperature, the phonon-phonon scattering
should increase as a step function at the temperature cor-
responding to the mode frequency, rather than showing a
peak. The observed peaks imply a strong temperature
dependence of the anharmonicity near the temperatures
corresponding to the mode frequencies. There is evi-
dence that the Ba atoms first shift toward and then away
form Cu-O planes as the temperature decreases from 250
to 80 K.[23] Thus, the phonon-phonon interaction has
maxima near the mode frequencies, and hence, so does
the acoustic attenuation.

Since lattice parameters of the YBa$_2$Cu$_3$O$_x$ change by
at most 1% when the oxygen concentration is reduced
from $x = 7$ to $x = 6$, all the phonon structures should
remain almost the same. Reports on infrared studies of
YBa$_2$Cu$_3$O$_x$ with various oxygen concentrations also
show little difference in the phonon modes.[21] Thus, the
attenuation of acoustic waves due to scattering by pho-
nons cannot change much over the entire range of oxygen
concentration. On the other hand, as film resistance in-
creases with increasing oxygen deficiency, the electric
field loss increases and eventually becomes dominant over
the phonon scattering loss.

The electric field coupling component of SAW attenua-
tion is determined by the ac resistance of the film, regard-
less of microscopic properties of the film. Nevertheless, it
provides us with valuable information about the nature of
charge transport in the base material of YBa$_2$Cu$_3$O$_x$ sys-
tem. Since, as discussed above, the SAW attenuation
probes more of the bulk material than the dc measure-
ment, more reliable low frequency ac resistance can be
obtained from the SAW attenuation data. In addition,
the electrical contact problem, which is often encoun-
tered in dc electrical measurements of high-temperature
superconductors, can be avoided by using the SAW tech-
nique.

Using Eq. (1) we have calculated ac resistance for sam-
ples H and I from the SAW attenuation data using the
same fitting parameter as in the previous paragraph.
They are plotted in Fig. 10 together with measured dc
resistance. For sample H in Fig. 10, the calculated resis-
tance agrees reasonably well with the measured one,
differing in magnitude by a factor of 2. For the state I,
no dc resistance is available because the contact resis-
tance is too high. Both calculated and measured resis-

TABLE II. Estimated parameters of sample $S2$ in the 3D
variable range-hopping model. In the estimation, $N(E_F)$
$= N_0(E_F)(x - 6)$ is used, where $N_0(E_F) = 4.8 \times 10^{28}$/eV m^3 (Ref.
20).

		L_l(Å)	L_H(Å)[a]	W_H(K)[a]
H	Measured	14	15	160
H	From $\alpha(T)$	19	16	130
I	From $\alpha(T)$	12	19	240

[a]Calculated at room temperature.

tance curves for H and I increase rapidly at low tempera-
tures, indicating some type of thermal activation of
charge carriers. Among the various models we have ex-
amined in order to explain the temperature dependence
of the curves in Fig. 10, Mott's variable range hopping
model[24] fits the data best.

In the variable range-hopping regime, where electron
localization is comparable to thermal activation, resis-
tance is determined by a temperature-dependent hopping
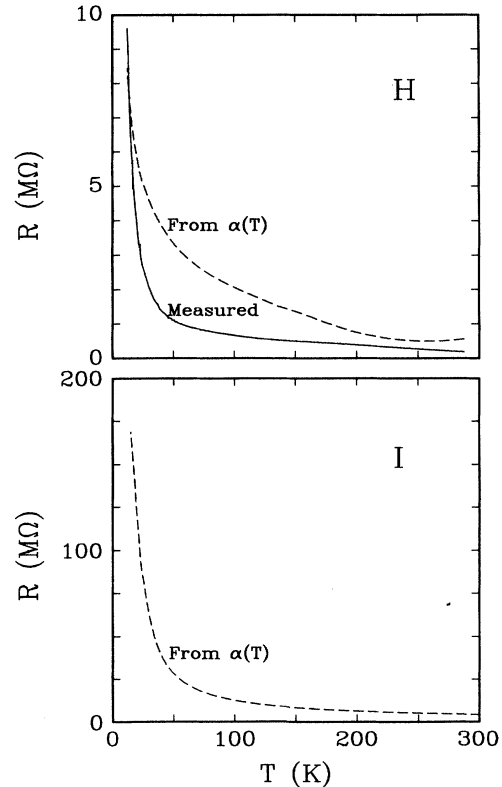distance, L_H, as[24]

FIG. 10. Temperature dependence of the film resistance,
both measured and calculated from SAW attenuation curves,
for H and I of the sample $S2$. dc resistance curve for I is not
available due to high contact resistance.

$$R = R_0 \exp(T_0/T)^{1/4} , \qquad (3)$$

with

$$k_B T_0 = \frac{24}{\pi} \frac{1}{L_l^3 N(E_f)} \quad \text{and} \quad L_H = \left[\frac{3L_l}{2\pi N(E_F)k_B T} \right]^{1/4} ,$$

where L_l is the localization length and $N(E_F)$ is density of states at the Fermi surface. The equations above are results for three dimensions. For 2D and 1D systems, the exponents in Eq. (3) are 1/3 and 1/2, respectively. Among these, the 3D model seems to give the best fit.

In Fig. 11 the curves in Fig. 10 are replotted with the resistance on a logarithmic scale versus $T^{-1/4}$. All the curves have linear slopes over a wide range of temperature. From the slopes L_l, L_H, and hopping energy $W_H = 3/[4\pi L_H^3 N(E_F)]$ are calculated using equations above. These parameters are given in Table II. Notice that hopping distances shown in Table II are larger than c-axis lattice parameter. Thus, it it consistent that the oxygen-deficient samples show a 3D hopping nature. This stands in contrast to 2D behavior of many electrical transport properties of fully oxygenated samples which are characterized by a short coherence length. Also, both localization, $\exp(2L_H/L_l)$, and thermal activation, $\exp(W_H/k_B T)$, contributions to the resistance are comparable, confirming that the system is indeed in the variable-range-hopping regime. Kastner et al.[25] have studied the temperature-dependent resistance of ceramics and crystals of Li-doped and -undoped La compounds. Room-temperature resistivity of their samples ranges from $10^{-2}\ \Omega\,cm$ to $5\times10^2\ \Omega\,cm$. All their data are also well explained by 3D Mott variable-range hopping.

In summary, we have studied epitaxial $YBa_2Cu_3O_x$ films for the entire range of oxygen concentration from $x = 6$ to $x = 7$ by a surface-acoustic-wave technique. In fully oxygenated films, the acoustic attenuation shows two broad peaks near temperatures of 135 and 240 K and an overall decay with decreasing temperature. These structures are most likely due to scattering of acoustic waves by optical phonons. None of our data have shown a gap structure at T_c, consistent with a relatively small effect of the electron-phonon interaction. In the semiconducting regime of the oxygen-deficient samples, SAW attenuation is predominantly due to the electrical-field coupling loss. The electrical-field coupling loss is determined by ac resistance of the film and reaches a maximum at
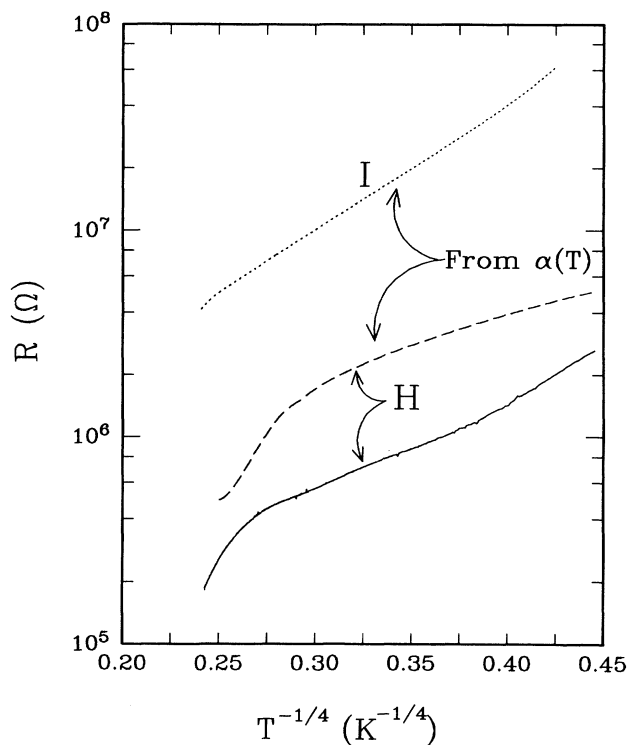

FIG. 11. The same curves as in Fig. 9 are replotted as R (on log scale) vs $T^{-1/4}$. Note that the curves are linear over a wide range of temperature.

$R_\square \approx 270\ k\Omega$. This field effect allows us to study the conduction mechanism in the base material of $YBa_2Cu_3O_x$ systems. Temperature-dependent resistance data, both measured dc and calculated ac, near the tetragonal phase are well explained by a 3D Mott variable-range-hopping model. Estimated hopping distances at room temperature are 15–20 Å. Further studies, such as magnetic field effects or investigation of single crystals, are needed to provide better understanding of high-temperature superconductors in the low-dopant limit.

ACKNOWLEDGMENTS

[1] R. W. Morse and A. V. Bohm, Phys. Rev. 108, 1094 (1957).

[2] See, for example, M. Tinkham, Introduction to Superconductivity (McGraw-Hill, New York, 1975), p. 53.

[3] Y. Horie, Y. Terashi, H. Fukuda, T. Fukami, and S. Mase, Solid State Commun. 64, 501 (1987).

[4] S. Bhattacharya, M. J. Higgins, D. C. Johnston, A. J. Jacobson, J. P. Stokes, J. T. Lewandowski, and D. P. Goshorn, Phys. Rev. B 37, 5901 (1988).

[5] M-F. Xu, D. Bein, R. F. Wiegart, B. K. Sarma, M. Levy, Z. Zhao, S. Adenwalla, A. Moreau, Q. Robinson, D. L. Johnson, S.-J Hwu, K. R. Poeppelmeier, and J. B. Ketterson, Phys. Rev. B 39, 843 (1989).

[6] M. Saint-Paul, J. L. Tholence, P. Monceau, H. Noel, J. C. Levet, M. Potel, P. Gougeon, and J. J. Capponi, Solid State Commun. 66, 641 (1988).

[7] X. D. Shi, R. C. Yu, Z. Z. Wang, N. P. Ong, and P. M. Chaikin, Phys. Rev. B 39, 827 (1989).

[8] T. J. Kim, J. Kowalewski, W. Assmus, and W. Grill, Z. Phys. B 78, 207 (1990).

[9] F. Akao, Phys. Lett. 30A, 409 (1969).

[10] S. G. Lee, G. Koren, A. Gupta, A. Segmüller, and C. C. Chi, Appl. Phys. Lett. 55, 1261 (1989).

[11] R. J. Cava, B. Batlogg, C. H. Chen, E. A. Rietman, S. M. Zahurak, and D. Werder, Phys. Rev. B 36, 5719 (1987).

[12] E. D. Specht, C. J. Sparks, A. G. Dhere, J. Brynestad, O. B. Cavin, and D. M. Kroeger, Phys. Rev. B 37, 7426 (1988).

[13]B. G. Orr, H. M. Jaeger, A. M. Goldman, and C. G. Kuper, Phys. Rev. Lett. **56**, 378 (1986).

[14]D. J. Werder, C. H. Chen, R. J. Cava, and B. Batlogg, Phys. Rev. B **38**, 5130 (1988).

[15]D. de Fontaine, M. E. Mann, and G. Ceder, Phys. Rev. Lett. **63**, 1300 (1989).

[16]See, for example, S. Datta, *Surface Acoustic Wave Technique* (Prentice-Hall, Englewood Cliffs, New Jersey, 1986).

[17]R. Adler, IEEE Trans. Sonics Ultrasonics **SU-18**, 115 (1971).

[18]See, for example, J. R. Schrieffer, *Theory of Superconductivity* (Benjamin, Reading, Massachusetts, 1964), p. 62.

[19]J. Callaway, *Quantum Theory of the Solid State* (Academic, New York, 1974), p. 639.

[20]J. Bardeen, D. M. Ginsberg, and M. B. Salamon, in *Novel Su-* *perconductivity*, edited by S. A. Wolf and V. Z. Kresin (Plenum, New York, 1987), p. 333.

[21]G. Burns, F. H. Dacol, P. P. Freitas, W. König, and T. S. Plaskett, Phys. Rev. B **37**, 5171 (1988).

[22]R. T. Collins, Z. Schlesinger, F. Holtzberg, and C. Field, Phys. Rev. Lett. **63**, 422 (1989).

[23]J. Konstantinovic, G. Parette, Z. Djordjevic, and A. Manelle, Solid State Commun. **70**, 163 (1989).

[24]N. F. Mott and E. A. Davis, *Electronic Processes in Non-Crystalline Materials* (Clarendon, Oxford, 1979), p. 32.

[25]M. A. Kastner, R. J. Birgeneau, C. Y. Chen, Y. M. Chiang, D. R. Gabbe, H. P. Jenssen, T. Junk, C. J. Peters, P. J. Picone, T. Thio, T. R. Thurston, and H. L. Tuller, Phys. Rev. B **37**, 111 (1988).